

Ms 8073 Revision 1

Oxidation or cation re-arrangement? Distinct behavior of riebeckite at high temperature

Giancarlo Della Ventura^{1,2,3}, Günther J. Redhammer⁴, Federico Galdenzi^{1,2},
Gennaro Ventruti⁵, Umberto Susta¹, Roberta Oberti⁶, Francesco Radica^{1,2}
and Augusto Marcelli^{2,7}

1 Dipartimento di Scienze, Università di Roma Tre, L. S. Leonardo Murialdo 1, 00146, Rome

2 INFN-LNF, Via E. Fermi 40, Frascati 00044 (Rome)

3 INGV, Via di Vigna Murata 605, 00143 Rome

4 University of Salzburg, Department Chemistry Physics of Materials, Jakob-Haringerstr. 2A, 5020 Salzburg, Austria.

5 Dipartimento di Scienze della Terra e Geoambientali, Università di Bari

6 CNR-Istituto di Geoscienze e Georisorse, sede secondaria di Pavia, via Ferrata 1, I-27100 Pavia, Italy

7 Rome International Centre for Material Science Superstripes - RICMASS, Via dei Sabelli 119A, 00185 Rome, Italy

ABSTRACT

In this work we address the stability of riebeckite at high temperature, and compare the different behaviors observed under different oxidation conditions. To this purpose, we annealed powders of a sample from Mt. Malosa (Malawi), which is compositionally close to the end member; the run products obtained after annealing in air *vs.* in vacuum were studied by Mössbauer spectroscopy and powder X-ray diffraction. The results show that riebeckite follows two distinct paths depending on the external environment. Under oxidizing conditions, it is stable in the hydrous form up to relatively low temperatures (400-450°C), then it undergoes a rapid (within ~50°C) dehydrogenation forming oxo-riebeckite which is stable up to ~900 °C. The final break-down products of the oxo-amphibole include aegirine +

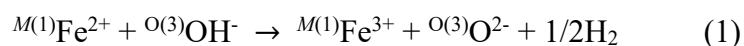
crystalite + hematite. Based on the relative intensity of the (310) Bragg reflection, the activation energy (E_a) for the riebeckite \rightarrow oxo-riebeckite transition is 166 ± 6 kJ/mol. Under vacuum conditions, no Fe oxidation is observed, and riebeckite is stable up to much higher temperatures (750-800°C); however, in the $550 < T < 700^\circ\text{C}$ range it undergoes a significant rearrangement of the C cations (those hosted in the strip of octahedra). Indeed, the amphibole stable in the 700-800 °C range has the same chemical formula as riebeckite, but has a disordered and non-standard cation distribution at the octahedra, i.e. $M^{(1)}(\text{Fe}^{3+}\text{Fe}^{2+})M^{(2)}(\text{Fe}^{3+}\text{Fe}^{2+})M^{(3)}\text{Fe}^{2+}$; we call this phase “ $\text{C}^{\text{R}^{3+}}$ disordered riebeckite”. For $T \geq 800$ °C, it decomposes to aegirine + fayalite + cristobalite + H_2O .

External oxygen is required for the release of water into the surrounding system, being a pre-requisite for the Fe-amphiboles to be a carrier of H_2O in the lower crust and upper mantle. One important implication of our results is that characterization of the overall oxidation state of iron does not necessarily provide the redox conditions of the environment of formation, because a crystal-chemical rearrangement under reducing conditions allows riebeckite to maintain its $\text{Fe}^{3+}/\text{Fe}^{2+}$ composition up to higher temperatures.

Key words: riebeckite, HT experiments, vacuum conditions, Mössbauer spectroscopy, X-ray powder diffraction

INTRODUCTION

Riebeckite, ideally $\text{Na}_2(\text{Fe}^{2+}_3\text{Fe}^{3+}_2)\text{Si}_8\text{O}_{22}(\text{OH})_2$, is a relatively common iron-rich member of the sodic amphibole subgroup; it is typically found in acid igneous rocks and as an important constituent of high-grade shists and meta-iron stones (Deer et al. 1997). The phase relations of riebeckite in the system $\text{Na}_2\text{O}-\text{FeO}-\text{SiO}_2-\text{H}_2\text{O}$ under hydrothermal conditions have been experimentally determined by Ernst (1962, 1968) at varying oxygen fugacity, temperature and pressure. According to these studies, end-member riebeckite is stable below $\sim 500^\circ\text{C}$, 1000 bars at f_{O_2} defined by the hematite-magnetite buffer; the effect of pressure was found to be rather limited with the stability increasing to $\sim 600^\circ\text{C}$ at 2 kbar. The breakdown product included hematite + magnetite + quartz + acmite + fluid (Ernst 1962). Under more reducing conditions (magnetite-quartz-fayalite buffer) the stability of the amphibole increases to $\sim 700^\circ\text{C}$ at 1 kbar. The fibrous form of riebeckite is the asbestos mineral known as “crocidolite”. Several studies on the thermal stability of crocidolite were done mostly in the 1960s and 1970s (see Della Ventura et al. 2018, 2021 for a complete list of references) mainly because crocidolite was used for efficient fire-resistant textiles. These studies were focused on the products of decomposition of crocidolite as a function of temperature, both in air and under inert (Ar , N_2) atmosphere. In particular, Hodgson et al. (1965) and Whitefield and Freeman (1967) observed the appearance, at $500\text{--}600^\circ\text{C}$ in N_2 atmosphere, of a modified amphibole phase named “crocidolite anhydrite”; the structural details of this phase were not determined. Under oxidizing conditions, the formation of “oxycrocidolite” was observed at $300\text{--}450^\circ\text{C}$ by Whitefield and Freeman (1967). The amphibole transformations under reducing conditions were also investigated by Addison and Sharp (1962) as well as the kinetics of H diffusion (Addison et al. 1962; Clark and Freeman 1967). The oxidation dynamics of iron in riebeckite during thermal annealing in air has been studied in detail by using a multi-methodological approach combining single-crystal structure refinement (SREF) with FTIR, Raman, XAS and Mössbauer spectroscopy (Oberti et al. 2018; Della Ventura et al. 2018, 2021; Galdenzi et al. 2018); the process can be described by the simple reaction:



whereby ferrous iron at the $M(1)$ site is oxidized to ferric iron, the local charge balance being maintained by the loss of H^+ ions at the anionic $O(3)$ site (Oberti et al. 2018). However, Della Ventura et al. (2018) showed that Fe-oxidation in riebeckite is indeed a much more complex process that depends strongly on the thermal range: (I) up to 450°C , Fe oxidation is

reversible; in the Raman spectra collected *in situ* during the annealing experiments the O-H stretching signal disappears, and peaks assigned to Fe³⁺-O modes appear. However, when the sample is quenched at RT, the O-H signal is recovered, and the ferric iron reduces to ferrous iron. We must conclude that in this T range both electrons (*e*⁻) and hydrogen cations (H⁺) are delocalized but remain within the amphibole matrix. (II) In the T interval 450-550°C, all ferrous iron irreversibly oxidizes to ferric iron, as indicated by Mössbauer spectroscopy and by the definitive collapse of the unit-cell parameters (Oberti et al. 2018; Della Ventura et al. 2018). Raman spectroscopy done on cooling also shows irreversible modifications of the lattice modes and the final disappearance of the O-H stretching signal. Therefore, the thermal energy supplied to the system is high enough for the expulsion of both the electrons and the protons from the structure. However, FTIR spectra collected in transmission through the crystal still show the presence of residual OH in the matrix core, implying that dehydrogenation starts at the surface of the sample, triggered by the presence of external oxygen. (III) At T > 550°C, FTIR spectroscopy is coherent with the total loss of H⁺, and thus with complete Fe oxidation. This process is irreversible, and the resulting oxo-amphibole is stable up to ~900°C (Oberti et al. 2018). The reversible oxidation of iron up to 450 °C had never been observed so far for other minerals, and might have important bearings in several other disciplines, including geophysics, toxicology and technology. It is worth of note that a similar behavior has recently been observed also in grunerite, ideally Fe²⁺₇Si₈O₂₂(OH)₂ (Mihailova et al. 2021).

The work described here was done to gain further insight into the oxidation of iron by direct measuring its valence state *via* Mössbauer spectroscopy on samples annealed at different temperatures and different redox conditions. The spectroscopic data were augmented by powder X-ray diffraction to follow the structure adjustments and identify the decomposition products with increasing T.

EXPERIMENTAL METHODS

The studied powders were obtained from cm-sized pegmatitic riebeckite crystals from Mt. Malosa, Zomba District (Malawi) described by Susta et al. (2018); the crystal-chemistry of the amphibole was fully characterized by using a combination of methods, including SREF, EMP, LA-ICPMS, FTIR, Raman and Mössbauer spectroscopies (Oberti et al. 2018, Della Ventura et al. 2018). The resulting composition is very close to that of the end-member $A^{\square}B^{\square}Na_2^C(Fe^{2+}_3Fe^{3+}_2)^T Si_8O_{22}^W(OH)_2$ (Oberti et al. 2018), the solid-solution observed implying

small amounts of ^{24}Mg (0.26 apfu) and ^{40}Ca (0.13 apfu), plus negligible ^{27}Al (0.11 apfu in total), ^{48}Ti (0.01 apfu) and ^{18}F (0.1 apfu).

Mössbauer spectra were collected at the University of Salzburg (Austria). Annealing was done in fused silica glass cells under dynamic high vacuum (HV) and slow evacuation down to $< 9 \cdot 10^{-6}$ mbar. After HV was reached, the temperature was increased at a rate of $10^\circ\text{C}/\text{min}$ to avoid strong particle movements, and the sample kept for 8 hours at the target T, during which the pressure was continuously monitored; it was always lower than 10^{-6} mbar and around 10^{-7} after the experiment. Finally, the cell was extracted from the furnace while under dynamic vacuum and allowed to cool to room-T. Transmission ^{57}Fe Mössbauer data were collected in air using an apparatus in horizontal arrangement (^{57}Fe Co/Rh single-line thin source, constant acceleration mode with symmetric triangular velocity shape, multi-channel analyzer with 1024 channels, regular velocity calibration against metallic Fe). Additional analyses were done using the same experimental apparatus on powders annealed in air at 450, 700 and 800°C for 8 hrs. The spectra were evaluated using the RECOIL program suite (Rancourt and Ping 1991; Rancourt et al. 1993, 1996); patterns were corrected for thickness effects and then processed using the full static hyperfine interaction Hamiltonian analysis with Lorentzian-shaped doublets.

X-ray powder diffraction (XPRD) data were collected on the same annealed samples subjected to Mössbauer spectroscopy by using a Bruker D8 system (Ni-filtered Cu - $K\alpha$ radiation, 0.3° divergence slits, 2.5° primary and secondary Soller slits, 1° anti-scatter slit) in combination with a Lynxeye detection system. Phase analysis was done using the EVA software package; quantitative phase analysis based on the Rietveld method was done using TOPAS V6.

In situ HT X-ray powder diffraction patterns were collected in the 2θ range $8-75^\circ$ with steps of 0.013° at the Geology Department of the University of Bari, with an Empyrean PANalytical diffractometer operating in Bragg-Brentano geometry and equipped with a high temperature (HT) cell (Anton Paar, model HTK 1200N) using Ni-filtered Cu $K\alpha$ radiation and a PIXcel linear detector. The sample was heated from RT to 800°C and then cooled back to RT always using a $10^\circ\text{C}/\text{min}$ rate. Patterns were collected at RT, 100, 200°C , every 25°C from 250 to 500°C , at 550, 600, 700 and 800°C and then every 100°C during cooling. The entire experiment lasted ~ 35 hours. Whole-pattern data were refined by the Le Bail method using a General Structure Analysis System software (Larson and Von Dreele 2000).

Three sets of isothermal heating experiments were done in air at 400, 425 and 450°C to study the riebeckite – oxo-riebeckite transition kinetics. Finely crushed riebeckite powder

was transferred in a pre-heated Nabertherm furnace, and temperature was held for different time, from 0.5 to 24 hours. At the end of the experiment, the powder was extracted from the furnace and cooled in air, and then analyzed via XRPD.

EXPERIMENTAL RESULTS

Heating in vacuum: Mössbauer spectroscopy

Selected refined ^{57}Fe Mössbauer spectra are shown in Figure 1 while all collected spectra can be found in the supplementary materials (Fig. S1); refined parameters are listed in Table 1. The RT spectrum of riebeckite was already described in Susta et al. (2018) and Oberti et al. (2018). It shows four well separated resonance absorption lines with two additional shoulders, and can be satisfactorily fit using three doublets corresponding to Fe^{2+} at the $M(1)$ and $M(3)$ sites, and to Fe^{3+} at the $M(2)$ site, respectively. All spectral features can be perfectly matched with this 3-doublet fit. Hence, there is no evidence for Fe^{2+} at $M(2)$, which is mainly occupied by Fe^{3+} . Also, there is no evidence for Fe^{2+} at the $M(4)$ site. Upon annealing in vacuum and *ex-situ* analysis, no change in the spectra is observed up to 500°C (Table 1).

At 550°C very small shoulders appear at ~ 1 mm/s and ~ 1.8 mm/s. They are too weak to be fitted, but their positions suggest that at least two new doublets are now required to model the pattern. Hence, in the sample annealed at 600°C two additional doublets were introduced. Based on their isomer shifts, they can be undoubtedly assigned to ferrous and ferric iron in octahedral coordination, respectively. The doublet assigned to Fe^{3+} has a larger quadrupole splitting (QS) than that assigned to Fe^{3+} at $M(2)$, while the doublet assigned to Fe^{2+} has a smaller QS than that assigned to Fe^{2+} at $M(1)$; both features are indicative of a more distorted local environments around the Fe probe nuclei (Della Ventura et al. 2016). These new spectral features are still weak in the sample annealed at 600°C but become much more intense in the samples annealed at 650°C and 700°C (Fig. 1).

A visual representation of the data from Table 1 (Fig. 2) shows that annealing under vacuum does not produce any variation in the relative $\text{Fe}^{3+}/\text{Fe}^{2+}$ site distribution up to 550°C . In the $550^\circ < T < 700^\circ\text{C}$ range, whereas the fraction of $M(3)\text{Fe}^{2+}$ remains constant around 20% of total iron and that of $\text{Fe}^{3+}_{\text{tot}}$ only slightly increases above 40 %, the amounts of $M(1)\text{Fe}^{2+}$ and $M(2)\text{Fe}^{3+}$ decrease significantly. We conclude that very limited Fe oxidation is accompanied by a significant cation exchange: $M(1)\text{Fe}^{2+}$ migrates to $M(2)$ and the same amount of $M(2)\text{Fe}^{3+}$ migrates to $M(1)$. Because the relative intensities of the two new doublets are almost equal, and their increase fits well the decrease of $M(2)\text{Fe}^{3+}$ and $M(1)\text{Fe}^{2+}$, we assign the two new

doublets appeared during thermal annealing under vacuum to $M(2)Fe^{2+}$ and $M(1)Fe^{3+}$, respectively (Table 1). In summary, in the $550^{\circ} < T < 700^{\circ}C$ range the Fe^{3+}/Fe^{2+} ratio in the amphibole remains almost constant, but the site partitioning of CFe changes from $M(1)Fe^{2+}_2M(2)Fe^{3+}_2M(3)Fe^{2+}$ to $M(1)(Fe^{3+}Fe^{2+})M(2)(Fe^{3+}Fe^{2+})M(3)Fe^{2+}$, ferric iron being equally disordered over $M(1)$ and $M(2)$. According to the rules in force (Hawthorne et al. 2012), the name of the amphibole depends on the overall composition at the various group-sites, and hence the products must yet be named “riebeckite”. However, the cation distribution is absolutely non-standard (Fe^{3+} strongly orders at $M(2)$ in amphiboles in the absence of the oxo-component, see Hawthorne and Oberti 2007); therefore we will name this phase “ ${}^CR^{3+}$ disordered riebeckite” in the following.

An important point to consider here is that, provided there is no Fe^{3+} short-range ordering at $M(1)$, all local arrangements close to the hydroxyl group in ${}^CR^{3+}$ disordered riebeckite are still of the type $M(1)Fe^{2+}_2M(1)Fe^{3+}_2M(3)Fe^{2+}-OH$ (see Fig. 3). This being the case, there is no need for a loss of protons. In fact, 0.17 extra valence units converging on the hydroxyl oxygen O(3) can be easily accommodated by bond-length adjustments. The same feature is observed in pargasite, where trivalent cations such as Al may distribute between the $M(2)$ and the $M(3)$ sites in Mg-rich samples (Oberti et al. 1995; Della Ventura et al. 1999; Della Ventura et al., 2003; Hawthorne and Della Ventura, 2007). Actually, IR spectroscopy shows no OH loss in riebeckite powders heated at HT in inert atmosphere even for prolonged time (Della Ventura et al. 2018, 2021).

X-ray diffraction (see below) shows that the sample annealed at $800^{\circ}C$ consists of minor residual riebeckite (~20%) and large amounts of clinopyroxene [aegirine ($NaFe^{3+}Si_2O_6$) and ferrosilite ($Fe^{2+}_2Si_2O_6$)]. As deduced from lattice parameters, the aegirine probably contains some Ca, and thus an equal amount of Fe^{2+} , a suggestion that is also supported by the Mössbauer refinement (Table 1). In fact, the spectrum collected after annealing at $800^{\circ}C$ can only be evaluated by using two doublets for Fe^{2+} at the M1 and M2 sites in ferrosilite, and three doublets (one for Fe^{3+} and two for Fe^{2+}) in aegirine, which are typical for pyroxenes along the hedenbergite – aegirine join (Redhammer et al. 2006). A weak Fe^{3+} component is also required, which has Mössbauer parameters similar to those of the additional Fe^{3+} component [$M(1)Fe^{3+}$] in the amphibole, and which should be assigned to riebeckite. Due to the large overlap, however, there is no clear evidence for the additional Fe^{2+} component [$M(2)Fe^{2+}$] to be assigned to riebeckite. For the ferrosilite phase, the two doublets have almost equal area fractions (as expected from stoichiometry), and the Mössbauer parameters agree very well with those given for $FeSiO_3$ by Dyar et al. (2013). Very similar conclusions apply to the

sample annealed at 900°C. Again, the signatures of ferrosilite and aegirine are dominant, and a broad 6th doublet can further improve the fit. Its hyperfine parameters are similar to the additional Fe³⁺ component in the amphibole; however, due to severe overlap its relative area fraction (~ 7%) is likely to be inaccurate.

Heating in air: Mössbauer spectroscopy

The evolution of the Fe³⁺/Fe_{tot} ratio in riebeckite heated in air up to 550°C was described by Oberti et al. (2018) by combining single-crystal structure refinement and Mössbauer spectroscopy. Those data are complemented by the new analyses done on powders annealed at 450, 750 and 800°C for 8 hrs (Fig. 4). Based on the data of Oberti et al. (2018), the presence of a significant amount of oxo-amphibole is expected for our experiments after 8 hrs annealing at 450°C. Indeed, the Mössbauer spectrum shows a distinct reduction in Fe²⁺ content, especially at the *M*(1) site (~3.2 % of total iron, Table 2), while the amount of Fe²⁺ at *M*(3) remains almost the same as in the untreated sample. However, a distribution of quadrupole splittings (QSD) was used to model the contribution of ^{*M*(3)}Fe²⁺ because some broadening is observed toward higher QS values with the components centered at 1.987(6) and 2.374(6) mm/s; the average <QS> value is thus given in Table 2. To evaluate the Fe³⁺ resonance absorption correctly, three components are required, and the inner two are assigned to the *M*(2) site as they sum up to 39 % of total iron (the value expected for the *M*(2) site), whereas the outer component is assigned to ^{*M*(1)}Fe³⁺. The final fit (Figure 4) was done using the QSD approach also for ^{*M*(2)}Fe³⁺, where the two components are centered at 0.540(5) and 0.885(5) mm/s at a ratio of 0.55 and 0.45, summing up to the <QS> of 0.689(5).

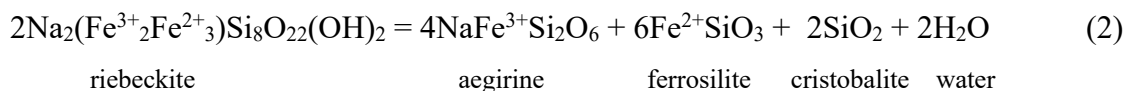
At 750°C and 800°C almost all Fe²⁺ is oxidized, the residual 12% is assigned to the *M*(3) site; we must conclude that at very high temperatures, also the *M*(3) site is involved in the oxidation process as already observed by Ernst and Wai (1970). The Fe²⁺ contribution in the spectrum can be modelled with one single doublet for Fe²⁺ at *M*(3), but the scenario is far more complex for Fe³⁺. The broad absorption related to Fe³⁺ might be interpreted based on two doublets plus a small shoulder around +0.65 mm/s. However, two broad shoulders around -0.7 mm/s and +1.5 mm/s suggest an additional doublet, the isomer shift of which is typical of ferric iron, whereas the QS is very large (~ 2.25 mm/s). When using such a three-doublet model, the innermost part of the spectrum around 0.4 mm/s cannot be fitted satisfactorily, and the two main Fe³⁺ components have area fractions far from those expected from the stoichiometry of oxo-riebeckite. They are ~ 15 % and ~ 65 % of total iron for the inner and outer doublet, respectively, and the line width are very different from each other. When

introducing a fourth ferric iron component, rapid convergence is obtained, and the two main Fe^{3+} components have similar area fractions and line widths; their area fractions correspond to the expected site populations at the $M(1)$ and $M(3)$ sites. The newly introduced doublet has a small QS, indicating a rather regular octahedron that is occupied by 7.6 % of total iron; this value, added to the Fe^{2+} refined at the $M(3)$ site sums up rather well to the value expected at this site. In contrast, the broad doublet with the large QS of ~ 2.25 mm/s can be assigned to ferric iron in a very distorted local environment, as in poorly crystallized iron oxides present as additional phases. At 800°C , a further small decrease in the $M(3)\text{Fe}^{2+}$ content is observed, which scales with the increase of the relative area fraction of the innermost Fe^{3+} doublet, supporting its assignment to $M(3)\text{Fe}^{3+}$. The evolution of the $\text{Fe}^{3+}/\text{Fe}^{2+}$ fractions at the different sites in the full T range $300 < T < 800^\circ\text{C}$ is shown in Figure 5a where the data from Oberti et al. (2018), obtained after 3 hrs annealing, have been combined with the those obtained at higher temperature (700°C and 800°C , 8 hrs) during this work.

The complete transition to oxo-riebeckite at 450°C (Table 2) is - at first glance - in contrast to the data of Oberti et al. (2018), who noted only partial dehydrogenation at that temperature. However, during this work we used longer annealing times, which most probably explains the differences in the Fe^{3+} content, as graphically shown in Figure 5b where the new data at $T = 450^\circ\text{C}$ have been added to Figure 5a. Oberti et al. (2018) noted that Fe^{2+} oxidation starts at the $M(1)$ site, and our spectra (Fig. 4) show that a new and very intense $M(1)\text{Fe}^{3+}$ contribution with a QS values of $0.946(6)$ mm/s is indeed present after 8 hrs annealing at 450°C . At these conditions, the samples undergo almost complete $M(1,2)\text{Fe}^{2+} \rightarrow M(1,2)\text{Fe}^{3+}$ transformation, the $M(3)$ site being virtually unaffected (Table 2). Annealing at higher temperatures shows that about half $M(3)\text{Fe}^{2+}$ is oxidized at 800°C ; interestingly, the QS values for the doublet used to gain convergence has a lower QS, suggesting that $M(3)\text{Fe}^{3+}$ occurs in a more regular octahedral environment. Viceversa, the QS for $M(1)\text{Fe}^{3+}$ increases towards $1.126(2)$ mm/s at 800°C , indicating a more distorted coordination geometry.

Information from powder X-ray diffraction

The powders annealed in vacuum were examined using X-ray diffraction after each Mössbauer data collection. Phase analysis by the Rietveld method confirms that riebeckite is the only phase present up to 700°C ; at 800°C only minor riebeckite ($\sim 20\%$) is left (Table 3) and most of the sample has transformed into aegirine (ae) + ferrosillite (fs) + cristobalite (cri), according to the (ideal) reaction:



At 900°C, no clear evidence of riebeckite is found, and the powder is a mixture of aegirine (67%), ferrosilite (30%), and traces of cristobalite (Table 3). Table S1 (in the supplementary) shows a small decrease in all the unit-cell edges with increasing temperature. A comparison of the lattice parameters refined for aegirine formed during the heating experiment (Table S1) with those obtained for phases synthesized along the join hedenbergite (hd) $\text{CaFe}^{2+}\text{Si}_2\text{O}_6$ – aegirine (ae) $\text{NaFe}^{3+}\text{Si}_2\text{O}_6$ join (Redhammer et al. 2006), suggests that its chemical composition is close to $\text{Ae}_{85}\text{Hd}_{15}$. Hence, the minor Ca present in riebeckite (see Oberti et al. 2018) is incorporated into aegirine; note that the presence of Ca in aegirine requires that of an equal amount of Fe^{2+} to obtain electroneutrality (as discussed in the Mössbauer section).

To check for the difference due to the annealing atmosphere, we did a series of quenching experiments in air (8 hours) and collected the XRPD patterns *ex-situ* at steps of 50°C in the $300 < T < 900^\circ\text{C}$ range. The relative phase contents measured in the powder during this second experiment are also shown in Table 3. The XRPD pattern measured after annealing at 400°C showed a splitting (Fig. 6) of the prominent peak at 28.5° (indexed as 310), and a satisfactory evaluation of the X-ray pattern could only be obtained when using two different sets of parameters, corresponding to riebeckite and oxo-riebeckite, respectively, as structural input data. The same was true for the sample tempered at 425°C. Quantitative Rietveld analysis indicates that, in the sample at 400°C, the two amphiboles coexist roughly in a 1:1 ratio, while at 425°C the ratio is about 35 % riebeckite and 65 % oxo-riebeckite (Table 3). At 450°C, the sample is almost only oxo-riebeckite. Increasing the temperature up to 800°C does not induce any additional change to the XRPD pattern but for some peak shifts, indicative of slight changes in the lattice parameters. At 850°C, the first evidence for the decomposition of riebeckite were found through the appearance of aegirine and cristobalite, plus small amounts of hematite. At 900°C, the amphibole disappears, and the run product consists of a mixture of aegirine + hematite + cristobalite. All the unit-cell edges (Table S1, Fig. 7) decrease abruptly at 400 – 450°C; at higher T, there is a gradual decrease up to the break-down temperature.

The effect of time on the results was preliminarily verified by collecting XRPD data along the 425°C isotherm at successive intervals of 8 hrs (Fig. 6). As expected, the peak assigned to riebeckite decreased in intensity as a function of time, and oxidation is nearly complete after 32 hrs. The unit-cell parameters decrease with prolonged heating but stabilize above 24 hrs, hence we can assume that after 24 hrs no significant change occur in the

sample. Based on these tests, we collected XRPD patterns in the 25-35° 2 θ range along three isotherms as a function of time.

The structural study on riebeckite powders thermally treated in air was completed by monitoring *in situ* the evolution of X-ray patterns as a function of temperature. Figure 8a shows that, in the RT < T < 400°C range, the positions of the diffraction peaks shift gradually as a consequence of the thermal expansion of the unit cell. Between 425 and 450°C there is an abrupt change in the patterns: the (201) and (310) diffraction peaks are in fact suddenly displaced toward higher 2 θ values. Such shift is compatible with a major contraction of the unit-cell parameters. The unit-cell dimensions measured at increasing T values are listed in the supplementary materials (Table S2); the evolution of the unit-cell volume is shown in Figure 8b. According to Oberti et al. (2018), during the heating cycle (filled squares) the gradual increase in all the unit-cell dimensions up to 425°C is due to thermal expansion of the structure. From 425 to 450°C, there is a decrease in all the parameters. Above 450°C thermal expansion occurs, and has the same slope as in the first part of the experiment; analysis of the patterns shows the presence of oxo-riebeckite alone, at least up to 800°C. During the cooling cycle (dotted squares in Figure 8b) the unit-cell volume of oxo-riebeckite decreases linearly.

The kinetics of the riebeckite to oxo-riebeckite transition

Both the Mössbauer and the XRPD data discussed above show that in air the riebeckite to oxo-riebeckite transition occurs in the 400 – 450 °C temperature range, where both phases coexist (Figs. 6 and 8).

Della Ventura et al. (2021) addressed the kinetics of riebeckite dehydrogenation by using FTIR spectroscopy, and showed that H loss in powdered riebeckite can be modeled as a first order reaction. In this work, we studied the same transition by monitoring the intensity of the (310) diffraction peak (Fig. 6) at 400, 425 and 450 °C as a function of time.

A general discussion on the different approaches to kinetics is found in Hancock and Sharp (1972) or in Brown et al. (1980). For amphibole powders, the dehydrogenation process can be conveniently treated by using the Avrami-Erofeev equation that can be expressed as:

$$y = 1 - \exp(-f(t)) \text{ or } I_R = I_{sum} \cdot \exp(-f(t)) \quad (3)$$

where $y = 1 - I_R/I_{sum}$ is the fraction of oxo-riebeckite at time = t (min), I_R is the intensity of the (310) peak of riebeckite at time = t, I_{sum} is the sum the intensities of the (310) peaks of riebeckite and oxo-riebeckite at time = t; $f(t)$ is an exponential function (Avrami 1939). Della Ventura et al. (2021) used a slightly different equation:

$$I_R = I_{sum} \cdot \exp[-(k \cdot t)^m] \quad (4)$$

where the exponential function $f(t)$ is described by two parameters k and m . The coefficient k , the rate constant, describes the decreasing trajectory *vs.* the concentration of the reactant, while the exponential factor m is an empirical factor used to model the reaction mechanism; m close to 1.0 indicates first order reactions (Hancock and Sharp 1972)

An example of fitting this equation to our experimental XRPD data is given in Figure 9a and the resulting parameters are listed in Table 4. The temperature dependence of the rate constant k , as expressed by the Arrhenius equation (4), can be used to calculate the activation energy E_a (kJ/mol) for the transition from riebeckite to oxo-riebeckite:

$$k = A \cdot \exp\left(-\frac{E_a}{RT}\right) \quad (5)$$

where R is the universal gas constant (J/mol), T is the temperature in Kelvin and A is the pre-exponential factor. In this equation, the activation energy represents the limiting energy barrier for the reaction to proceed, while the pre-exponential factor is the reaction frequency (Galwey and Brown 1999). The rate constants k from Table 4 are plotted in the Arrhenius space (Fig. 9b) and the activation energy (E_a) is given by the slope of the regression line across the data points multiplied by R (the Boltzmann constant). In Figure 9b, the k values obtained during this work by monitoring the (310) peak in the XRPD patterns align with those obtained for riebeckite powders studied *via* FTIR spectroscopy by Della Ventura et al. (2021). Figure 9b thus shows that probing the same phenomenon from two distinct points of view, i.e., the structure adjustment due to the Fe oxidation (XRPD) and the loss of H^+ (FTIR) indicates that the two processes have the same energetics. The calculated E_a for the riebeckite to oxo-riebeckite transition using all data plotted in Figure 9b is 166 ± 6 kJ/mol.

CONCLUSIONS AND IMPLICATIONS

Riebeckite is a common rock-forming mineral under high-pressure metamorphic conditions (Deer et al. 1997), and the main asbestos mineral used in a large variety of technological applications for at least one century (Gunther et al. 2007).

The crystal chemistry of the amphiboles is controlled by a complex interconnection between the chemistry of the geological system (be it a rock subject to metamorphism, or a melt) and the P-T- f_{O_2/H_2O} conditions (see Martin 2007 and Schumacher 2007). The main crystal-chemical response to changes in boundary conditions is the loss of H^+ (dehydrogenation); accordingly, the first criterion presently used for classification in the amphibole supergroup is the relative amount of the W anions (OH^- , O^{2-}) in the general formula (Hawthorne et al. 2012).

There are two mechanisms controlling the OH^- content of the amphiboles:

- 1) Crystallization in the presence of ${}^C\text{Ti}$ (Oberti et al. 1992, Della Ventura et al. 2007, Oberti et al., 2015; Gatta et al., 2017; Liao et al. 2021); this feature is well known in amphiboles from mantle-related occurrences where the compositions are typically ${}^C\text{Ti}$ -rich and OH^- poor (Dyar et al. 1993).
- 2) oxidation of Fe according to equation (1) when T increases, for example during subduction.

Significant efforts have been made toward understanding how much the $\text{OH}^-/\text{O}^{2-}$ ratio in amphiboles is affected by the redox state of the mantle source and how much it is due to post-crystallization events, such as reactions during magma uplift to the surface and post-effusive oxidation (Dyar et al. 1993). An intriguing feature already observed in early experiments (Popp et al. 2006) and demonstrated by recent work (Della Ventura et al. 2018, Mihailova et al. 2021) is that equation (1) is reversible in a relatively broad range of temperatures; this is indeed an issue that has several implications, both in Geology/Geophysics and in Material Science.

The results of this work clearly show that the riebeckite may follow two totally different thermodynamic paths as a function of temperature. At oxidizing conditions, it is stable in the hydrous form up to relatively low temperatures; it undergoes a sudden transformation to oxo-riebeckite, which is completed within $\sim 50^\circ\text{C}$, and then is stable up to high-T ($\sim 800^\circ\text{C}$ for powders, this work and $\sim 900^\circ\text{C}$ for single-crystals: Oberti et al. 2018). X-ray diffraction shows a reduction of the unit-cell parameters in the $400\text{--}450^\circ\text{C}$ range (Fig. 7 and 8), with a significant contraction of the octahedra where Fe^{2+} oxidizes to Fe^{3+} (ionic radii: $\text{Fe}^{2+} = 0.78$ and $\text{Fe}^{3+} = 0.645 \text{ \AA}$, respectively, Shannon 1976) coupled with a simultaneous loss of H^+ in order to maintain local electroneutrality. These structural modifications cause a major decrease of the a edge (which is particularly sensitive to H^+ loss, see for example Robert et al. 1989) and of the b edge (which is particularly sensitive to the dimension of the octahedra, e.g. Colville et al. 1966).

The rate constants (k) measured at different temperature for the riebeckite to oxo-riebeckite transition at oxidizing conditions align (Fig. 9b) with those measured via FTIR by Della Ventura et al. (2021); this implies that the two techniques probe different aspects of the same process, that are strongly correlated. However, Figure 10 shows that the structural adjustment is virtually complete at 450°C whereas dehydrogenation needs higher temperature to be effective. This is in agreement with the observation of Della Ventura et al. (2018, 2021) and Mihailova et al. (2021) that the electronic transfer precedes and triggers the structural modifications and the final loss of H. The activation energy for dehydrogenation in riebeckite

is in agreement with previous data from the literature (Clark and Freeman 1967; Della Ventura et al. 2021).

According to equation (1), this transformation is strongly dependent upon the availability of external oxygen and, when this is the case, may lead to the release of water into the surrounding system. For this reason, Fe-amphiboles are considered among the main carriers of water in the lower crust and upper mantle. Note that in this process the amphibole provides H^+ and not water to the system (Hu et al. 2018; Mihailova et al. 2021). The final break-down products of the oxo-amphibole include aegirine + cristobalite + hematite. At 900°C, the transformation is virtually complete (Table 3).

Under vacuum, there is almost no Fe oxidation, and riebeckite is stable as a hydrous amphibole up to 700-750°C; in the XRPD patterns there is no evidence of transformation into an oxo-amphibole (i.e. no peak splitting, see above). However, in the 550<T<700°C range riebeckite undergoes a significant cationic rearrangement to ${}^C R^{3+}$ disordered riebeckite that, at 800 °C decomposes into aegirine + fayalite + cristobalite + H₂O. This scenario is clarified by the evolution of the Fe speciation and partitioning in riebeckite as a function of T provided by Mössbauer spectroscopy and summarized in Figure 10, where the stability ranges of riebeckite and ${}^C R^{3+}$ disordered riebeckite are shown. Oberti et al. (2018) found that the oxo-amphibole obtained by heating riebeckite in air had significant ${}^4 Na$, in agreement with experimental work showing that sodium amphiboles at high-*T* in oxidizing conditions deviate in composition towards arfvedsonite (Ernst 1962, 1968). Under reducing conditions such disorder does not occur. This study was done on powders, and hence we could not refine ${}^4 Na$ occupancy in the resulting amphiboles. However, we note that any migration of Na from the *M*(4) to the *A* site should imply migration of ${}^C Fe^{2+}$ to *M*(4), and Mössbauer spectroscopy shows that this is not the case.

The first geological implication of our work is that under reducing conditions, the stability limit of riebeckite (structurally speaking) is at least 100°C lower than under oxidizing conditions. Reducing conditions, on the other side, may stabilize pyroxene phase(s), and promote riebeckite breakdown.

The second important implication is that characterization of the overall oxidation state of iron does not necessarily provide the oxidation state of the environment of formation, because ${}^C R^{3+}$ disordered riebeckite is stable under reducing conditions and has the same Fe^{3+}/Fe^{2+} ratio of riebeckite. Therefore, a possible correlation between the oxidation state of the amphibole and the temperature, for any petrological reconstruction, must necessarily take

into consideration the cation site-distribution (i.e., the crystal-chemistry) as well as the $\text{Fe}^{3+}/\text{Fe}^{2+}$ ratio (i.e., the chemical composition) of the sample.

Regarding possible geophysical implications, this study shows that the different stability of OH-amphiboles vs. oxo-amphiboles must be taken into account when interpreting and extrapolating the conductivity data and the connection between polaron vs. ionic (fluid-mediated) conductivity (Hu et al. 2018).

Finally, the possible role of pressure in the HT processes involving Fe-amphiboles, and its consequences on oxidation/conduction have not been addressed during this work and data in the literature are extremely scarce. The early work of Ernst (1962, 1968) suggests that the role of pressure on the stability of riebeckites is negligible; however, our data definitively suggest that experimental studies aimed at clarifying the actual effect of pressure on the hydroxy-oxo transition in riebeckite, and more generally in amphiboles, are highly desirable. In this context it is worth considering the work of Burns et al. (1972) who studied via Mössbauer spectroscopy the pressure-induced change in the oxidation state of iron in a synthetic (Mg,Fe)-riebeckite. With increasing P, they observed a significant reduction of Fe^{3+} to Fe^{2+} in the sample; fitting of the Mössbauer spectra showed that Fe reduction occurred mainly at $M(3)$ up to 20 kbar, and at $M(1)$ for higher pressures. This result, which is not yet definitively clarified, further strengthens the connection between the role of the hydrogen bonded to O(3) in maintaining the local electroneutrality during iron oxidation/reduction.

Acknowledgement: We thank Gerold Tippelt (Salzburg) for help with Mössbauer data collection and Thomas Schwab (Salzburg) for the annealing experiments.

Financial support was provided by the Grant to Department of Science, Roma Tre University (MIUR-Italy Dipartimenti di Eccellenza, ARTICOLO 1, COMMI 314-337 LEGGE 232/2016). The final version of the work benefited of positive criticism by F.C. Hawthorne (Winnipeg, Manitoba) and an anonymous referee.

References

- Addison, W.E., and Sharp, J.H. (1962) Amphiboles. Part III. The reduction of crocidolite. *Journal of the Chemical Society*, 3693-3698.
- Addison, W.E., Neal, G.H., and Sharp, J.H. (1962). Amphiboles. Part II. The kinetics of oxidation of crocidolite. *Journal of the Chemical Society*, 1472-1475.
- Avrami M. (1939). Kinetics of Phase Change. I. General Theory. *Journal of Chemical Physics*, 7, 1103-1112.
- Brown, M.E., Dollimore D., Galwey A.K. (1980) *Reactions in the solid state*. Elsevier, Amsterdam.
- Burns, R.G., Tossell, J.A., Vaughan, D.J. (1972) Pressure-induced reduction of a ferric amphibole. *Nature*, 240, 33-35.
- Clark, M.W. and Freeman, A.G. (1967) Kinetics and mechanism of dihydroxylation of crocidolite. *Transaction of the Faraday Society*, 63, 2051-2056.
- Colville, P.A., Ernst, W.G., Gilbert, M.C. (1966) Relationships between cell parameters and chemical compositions of monoclinic amphiboles. *American Mineralogist*, 51, 1727–1754.
- Deer, W.A., Howie, R.A., Zussman, J. (1997): *Double-chain silicates* (second edition). The Geological Society, London, pp. 764.
- Della Ventura, G., Hawthorne, F.C., Robert, J.-L., Delbove, F., Welch, M.D., Raudsepp, M. (1999) Short-range order of cations in synthetic amphiboles along the richterite - pargasite join. *European Journal of Mineralogy*, 11, 79-94.
- Della Ventura, G., Hawthorne, F.C., Robert, J.-L., Iezzi, G. (2003) Synthesis and infrared spectroscopy of amphiboles along the tremolite – pargasite join. *European Journal of Mineralogy*, 15, 341-347.
- Della Ventura, G., Oberti, R., Hawthorne, F.C., Bellatreccia, F. (2007) Single-crystal FTIR study Ti-rich pargasites from Lherz: the spectroscopic detection of $^{03}\text{O}^{2-}$ in amphiboles. *American Mineralogist*, 92, 1645-1651.
- Della Ventura, G., Redhammer, G., Robert, J.L., Sergent, J., Iezzi, G., Cavallo, A. (2016) Crystal-chemistry of synthetic amphiboles along the join richterite - ferro-richterite: a combined spectroscopic (FTIR, Mössbauer), XRPD and microchemical study. *Canadian Mineralogist*, 54, 97-114.
- Della Ventura, G., Milahova, B., Susta, U., Cestelli Guidi, M., Marcelli, A., Schlüter, J., Oberti, R. (2018) The dynamics of Fe oxydation in riebeckite: a model for amphiboles. *American Mineralogist*, 103, 1103-1111.

- Della Ventura, G., Radica, F., Galdenzi, F., Susta, U, Cinque, G., Mihailova, B., Marcelli, A. (2021) Kinetics of hydrogen diffusion in riebeckite, $\text{Na}_2\text{Fe}^{3+}_2\text{Fe}^{2+}_3\text{Si}_8\text{O}_{22}(\text{OH})_2$: an HT-FTIR study. American Mineralogist, in press, doi.org/102128/am-2022-8021.
- Dyar, M.D., Macwell, S. J., McGuire, A.V., Cross, L.R. and Robertson, J. D. (1993) Crystal chemistry of Fe^{3+} and H^+ in mantle kaersutites: implications for mantle metasomatism. American Mineralogist 78, 968-979.
- Dyar, M.D., Klima, R.L., Fleagle, A. and Peel, S. E. (2013). Fundamental Mössbauer parameters of synthetic Ca-Mg-Fe pyroxenes. American Mineralogist 98, 1172-1186.
- Ernst, W.G. (1962) Synthesis and stability relations and occurrence of riebeckite and riebeckite-arfvedsonite solid solutions. Journal of Geology, 70, 689-636.
- Ernst, W.G. (1968) Amphiboles. Springer-Verlag, Berlin, 125 pp.
- Ernst, W.G. and Wai, M. (1970). Mössbauer, infrared, X-ray and optical study of cation ordering and dehydrogenation in natural and heat-treated sodic amphiboles. American Mineralogist 55, July-august, 1970. 1226-1258.
- Galwey A.K., Brown M.E. (1999) Thermal decomposition of ionic solids. Elsevier, Amsterdam.
- Galdenzi, F., Della Ventura, G., Cibin, G., Macis, S., Marcelli, A., (2018). Accurate $\text{Fe}^{3+}/\text{Fe}_{\text{tot}}$ ratio from XAS spectra at the Fe K-edge Radiation Physics and Chemistry. doi.org/10.1016/J.radphyschem.2018.12.008
- Gatta, G.D., McIntyre, G.J., Oberti, R., Hawthorne, F.C. (2017): Order of $^{[6]}\text{Ti}^{4+}$ in a Ti-rich calcium amphibole from Kaersut, Greenland: a combined X-ray and neutron diffraction study. Physics and Chemistry of Minerals 44, 83-94.
- Gunther, M.E., Belluso, E., Mottana, A. (2007) Amphiboles: environmental and health concerns. In F.C. Hawthorne, R. Oberti, G. Della Ventura and A. Mottana, Eds, Amphiboles: Crystal Chemistry, Occurrence and Health Issues, 67, 453-516. Reviews in Mineralogy and Geochemistry, Mineralogical Society of America, Chantilly, Virginia.
- Hancock J.D., Sharp J.H. (1972) Method of comparing solid-state kinetic data and its application to the decomposition of kaolinite, brucite, and BaCO_3 . Journal of American Ceramic Society, 55, 74-77.
- Hawthorne, F.C., Della Ventura, G. (2007) Short-range order in amphiboles. In F.C. Hawthorne, R. Oberti, G. Della Ventura and A. Mottana, Eds, Amphiboles: Crystal Chemistry, Occurrence and Health Issues, 67, 173-222. Reviews in Mineralogy and Geochemistry, Mineralogical Society of America, Chantilly, Virginia.

- Hawthorne, F.C. and Oberti, R. (2007) Amphiboles: crystal chemistry. In F.C. Hawthorne, R. Oberti, G. Della Ventura and A. Mottana, Eds, Amphiboles: Crystal Chemistry, Occurrence and Health Issues, 67, 1-54. Reviews in Mineralogy and Geochemistry, Mineralogical Society of America, Chantilly, Virginia.
- Hawthorne F.C., Oberti R., Harlow G.E., Maresch W.V., Martin R.F., Schumacher J.C., Welch M.D. (2012) Nomenclature of the amphibole supergroup. American Mineralogist, 97, 2031-2048.
- Hodgson, A.A., Freeman, A.G., and Taylor, H.F.V. (1965) The thermal decomposition of crocidolite from Koegas, South Africa. Mineralogical Magazine, 35, 1965. 5-29.
- Hu H., Dai L., Li H., Sun W., Li B. (2018) Effect of dehydrogenation on the electrical conductivity of Fe-bearing amphibole: Implications for high conductivity anomalies in subduction zones and continental crust, Earth and Planetary Science Letters, 498, 27-37.
- Johnson N.M., Fegley, B. (2003) Tremolite decomposition on Venus II. Products, kinetics, and mechanism. Icarus 164, 317-333.
- Larson, A.C., Von Dreele R.B. (2000) General Structure Analysis System (GSAS). Los Alamos National Laboratory Report LAUR 86-748.
- Liao, Y., Wei, C., Rehman, H.U. (2021) Titanium in calcic amphibole: behaviour and thermometry. American Mineralogist, 106, 180-191.
- Martin, R.F. (2007) Amphiboles in the igneous environment. In F.C. Hawthorne, R. Oberti, G. Della Ventura and A. Mottana, Eds, Amphiboles: Crystal Chemistry, Occurrence and Health Issues, 67, 325-358. Reviews in Mineralogy and Geochemistry, Mineralogical Society of America, Chantilly, Virginia.
- Mihailova B., Della Ventura, G., Waselmann, N., Xu, W., Schluter, J., Galdenzi, F., Marcelli, A., Redhammer, G. J., Boiocchi, M., Oberti, R. (2021) Coupled phonon-electron excitations in hydrous Fe-bearing silicates: a key to understanding lithospheric conductivity, Communication Materials, doi.org/10.1038/s43246-021-00161-y.
- Momma K., Izumi F. (2008) VESTA: a three-dimensional visualization system for electronic and structural analysis. Journal of Applied Crystallography, 41, 653-658.
- Oberti, R., Ungaretti, L., Cannillo, E., Hawthorne, F.C., (1992) The behaviour of Ti in amphiboles. Four - and six-coordinate Ti in richterite. European Journal of Mineralogy, 4, 425-440.
- Oberti, R., Hawthorne, F.C., Ungaretti, L., Cannillo, E. (1995) ⁶⁷Al disorder in amphiboles from mantle peridotite. Canadian Mineralogist, 33, 867-878.

- Oberti, R., Boiocchi, M., Hawthorne, F.C. & Cámara, F., Ciriotti, M., Berge, S.A. (2015): Ti-rich fluoro-richterite from Kariåsen (Norway): The oxo-component and the use of Ti^{4+} as a proxy. *Canadian Mineralogist* 53, 285-294.
- Oberti, R., Boiocchi, M., Zema, M., Hawthorne, F.C., Redhammer, G.J., Susta, U., Della Ventura, G. (2018) Understanding the peculiar HT behavior of riebeckite: expansivity, deprotonation, Fe-oxidation and a novel cation disorder scheme. *European Journal of Mineralogy*, 3, 437-449.
- Popp, R.K., Hibbert, H.A., Lamb, W.M. (2006) Oxy-amphibole equilibria in Ti-bearing calcic amphiboles: experimental investigation and petrologic implications for mantle-derived amphiboles. *American Mineralogist*, 91, 54-66.
- Rancourt, D.G., Ping, J.Y. (1991) Voigt-based methods for arbitrary-shape static hyperfine parameter distributions in Mössbauer spectroscopy. *Nuclear Instruments and Methods in Physics Research B (NIMB)* 58, 85–97.
- Rancourt, D.G., McDonald, A.M., Lalonde, A.E., Ping, J.Y. (1993) Mössbauer absorber thickness for accurate site populations in Fe-bearing minerals. *American Mineralogist*, 78, 1-7.
- Rancourt, D.G., Ping, J.Y., Boukili, B., Robert, J.-L. (1996) Octahedral-site Fe^{2+} quadrupole splitting distributions from Mössbauer spectroscopy along (OH, F)-annite join. *Physics and Chemistry of Minerals* 23, 63–71.
- Redhammer, G. J., Amthauer, G., Roth, G., Tippelt, G. & Lottermoser, W. (2006). *American Mineralogist* 91, 1271-1292.
- Robert, J.-L., Della Ventura, G., Thauvin, J.-L. (1989) The infrared OH-stretching region of synthetic richterites in the system $Na_2O-K_2O-CaO-MgO-SiO_2-H_2O-HF$. *European Journal of Mineralogy*, 1, 203-211.
- Shannon, R.D. (1976) Revised effective ionic radii and systematic studies of interatomic distances in halides and chalcogenides. *Acta Crystallographica*, A32, 751-767.
- Schumacher, J.C. (2007) Metamorphic amphiboles: composition and coexistence In F.C. Hawthorne, R. Oberti, G. Della Ventura and A. Mottana, Eds, *Amphiboles: Crystal Chemistry, Occurrence and Health Issues*, 67, 359-416. *Reviews in Mineralogy and Geochemistry*, Mineralogical Society of America, Chantilly, Virginia.
- Susta, U., Della Ventura, G., Hawthorne, F.C., Abdu, Y.A., Day, M.C., Mihailova, B., Oberti, R. (2018) The crystal-chemistry of riebeckite, ideally $Na^2Fe^{2+}_3Fe^{3+}_2Si_8O_{22}(OH)_2$: a multi-technic study. *Mineralogical Magazine*. 82, 837-852.

Withfield, H.J. and Freeman, A.G. (1967) Mössbauer study of amphiboles. *Journal of Inorganic Nuclear Chemistry*, 29, 903-914.

Table 1: Fitted ^{57}Fe Mössbauer parameters for the riebeckite powders annealed in vacuum.

Sample ID	IS δ mm/s	QS Δ mm/s	HWHM $\Gamma/2$ mm/s	A (%)	assignment
25°C initial	1.129(5)	2.874(2)	0.122(5)	39.0(6)	Fe ²⁺ M(1)
	1.130(7)	2.361(5)	0.139(4)	21.5(7)	Fe ²⁺ M(3)
	0.388(4)	0.465(2)	0.127(4)	39.5(3)	Fe ³⁺ M(2)
450°C	1.129(6)	2.871(3)	0.120(5)	38.7(7)	Fe ²⁺ M(1)
	1.131(5)	2.360(3)	0.125(4)	22.4(6)	Fe ²⁺ M(3)
	0.395(5)	0.456(4)	0.125(6)	38.9(4)	Fe ³⁺ M(2)
500°C	1.130(4)	2.866(4)	0.122(5)	38.0(6)	Fe ²⁺ M(1)
	1.127(5)	2.365(3)	0.153(4)	23.0(7)	Fe ²⁺ M(3)
	0.393(4)	0.463(3)	0.127(5)	39.0(4)	Fe ³⁺ M(2)
550°C	1.131(5)	2.860(4)	0.125(4)	38.2(7)	Fe ²⁺ M(1)
	1.124(6)	2.350(6)	0.149(6)	21.7(7)	Fe ²⁺ M(3)
	0.393(4)	0.467(4)	0.134(5)	40.2(5)	Fe ³⁺ M(2)
600°C	1.132(4)	2.859(5)	0.120(5)	31.8(8)	Fe ²⁺ M(1)
	1.125(5)	2.367(4)	0.147(6)	20.2(7)	Fe ²⁺ M(3)
	0.391(5)	0.465(4)	0.137(5)	35.4(4)	Fe ³⁺ M(2)
	0.457(4)	0.829(6)	0.218(6)	6.1(9)	Fe ³⁺ M(1)
	0.943(5)	1.93(7)	0.275(6)	6.5(9)	Fe ²⁺ M(2)
650°C	1.132(5)	2.849(6)	0.121(5)	26.9(7)	Fe ²⁺ M(1)
	1.131(6)	2.364(6)	0.171(6)	21.2(7)	Fe ²⁺ M(3)
	0.388(6)	0.458(4)	0.131(7)	26.4(5)	Fe ³⁺ M(2)
	0.393(5)	0.873(6)	0.220(7)	15.3(8)	Fe ³⁺ M(1)
	1.037(6)	1.719(6)	0.262(6)	10.3(9)	Fe ²⁺ M(2)
700°C	1.136(5)	2.843(7)	0.120(6)	21.3(6)	Fe ²⁺ M(1)
	1.134(6)	2.371(6)	0.172(5)	18.2(7)	Fe ²⁺ M(3)
	0.385(6)	0.487(5)	0.141(5)	23.0(5)	Fe ³⁺ M(2)
	0.407(5)	0.915(6)	0.176(6)	18.7(8)	Fe ³⁺ M(1)
	1.077(6)	1.767(8)	0.281(5)	18.8(8)	Fe ²⁺ M(2)
800°C	0.389(7)	0.353(2)	0.138(6)	27.3(9)	Fe ³⁺ M1 (ae)
	1.167(8)	2.820(4)	0.121(3)	6.7(1.8)	Fe ²⁺ M1 (ae)
	1.161(11)	2.147(4)	0.120(6)	7.4(1.9)	Fe ²⁺ M1 (ae)
	1.182(7)	2.532(3)	0.131(3)	18.1(8)	Fe ²⁺ M1 (fs)
	1.120(13)	1.890(6)	0.141(4)	21.5(9)	Fe ²⁺ M2 (fs)
	0.396(15)	0.884(8)	0.200(5)	19.1(1.0)	Fe ³⁺ M(1)
900°C	0.384(6)	0.380(4)	0.144(6)	35.6(9)	Fe ³⁺ M1 (ae)
	1.154(6)	2.848(5)	0.121(3)	6.3(9)	Fe ²⁺ M1 (ae)
	1.148(6)	2.130(3)	0.160(3)	15.4(9)	Fe ²⁺ M1 (ae)
	1.173(5)	2.537(4)	0.139(3)	18.0(6)	Fe ²⁺ M1 (fs)
	1.139(5)	1.849(4)	0.149(4)	17.3(7)	Fe ²⁺ M2 (fs)
	0.399(6)	0.899(3)	0.337(12)	7.3(8)	Fe ³⁺ M(1)

IS = isomer shift, QS = quadrupole splitting, HWHM = half width at half maximum (peak width), A = relative fraction of total iron, ae = aegirine, fs = ferrosilite.

Table 2: Fitted ^{57}Fe Mössbauer parameters for riebeckite powders annealed in air.

Sample ID	IS δ mm/s	QS Δ mm/s	HWHM $\Gamma/2$ mm/s	A (%)	site
450°C/ air	1.113(2)	2.791(7)	0.134(4)	3.2(9)	Fe^{2+} M(1)
	1.084(3)	2.064(6)*	0.155(4)	19.9(5)	Fe^{2+} M(3)
	0.378(2)	0.689(5)*	0.153(4)	39.3(6)	Fe^{3+} M(2)
	0.423(2)	0.946(6)	0.158(4)	37.6(8)	Fe^{3+} M(1)
750°C/ air	1.060(3)	2.087(6)	0.160(3)	12.3	Fe^{2+} M(3)
	0.404(1)	0.855(2)	0.171(1)	37.9	Fe^{3+} M(2)
	0.404(1)	1.087(2)	0.168(1)	37.9	Fe^{3+} M(1)
	0.385(3)	0.522(6)	0.113(2)	7.6	Fe^{3+} M(3)
	0.399(1)	2.248(9)	0.192(6)	4.2	Fe^{3+}
800°C/ air	1.045(3)	2.123(6)	0.160(3)	11.0	Fe^{2+} M(3)
	0.403(1)	0.854(2)	0.164(1)	37.4	Fe^{3+} M(2)
	0.396(1)	1.126(2)	0.157(1)	37.0	Fe^{3+} M(1)
	0.381(2)	0.527(4)	0.123(3)	9.1	Fe^{3+} M(3)
	0.377(1)	2.255(2)	0.221(2)	5.5	Fe^{3+}

* average QS in the quadrupole splitting distribution (QSD)

Table 3: Estimations of phase contents using the Rietveld method.

T (°C)	environment	OH-amph	oxo-	ae	fs	cri	hem
450	vac	100		--	--	--	--
500	vac	100		--	--	--	--
550	vac	100		--	--	--	--
600	vac	100		--	--	--	--
650	vac	100		--	--	--	--
700	vac	100		--	--	--	--
800	vac	21(4)		50(4)	28(3)	22(1)	--
900	vac	--		67(4)	30(3)	3(1)	--
300	air	100		--	--	--	
400	air	50	50	--	--	--	
425	air	35	65	--	--	--	
450	air	--	100	--	--	--	
500	air	--	100	--	--	--	
600	air	--	100	--	--	--	
700	air	--	100	--	--	--	
800	air	--	100	--	--	--	
850	air	--	49(2)	39(2)	--	9(1)	3(1)
900	air	--	--	58(2)	--	24(1)	18(1)

Table 4. Fitting parameters obtained using the Avrami equation for the isothermal experiment on riebeckite powders. The uncertainty on the last digit is given in brackets.

Temperature (°C)	<i>k</i>	<i>m</i>	-log <i>k</i>
450	0.0100 (5)	1.18 (7)	4.61 (3)
425	0.00317 (6)	0.82 (2)	5.75 (1)
400	0.00151 (5)	1.09 (5)	6.50 (2)

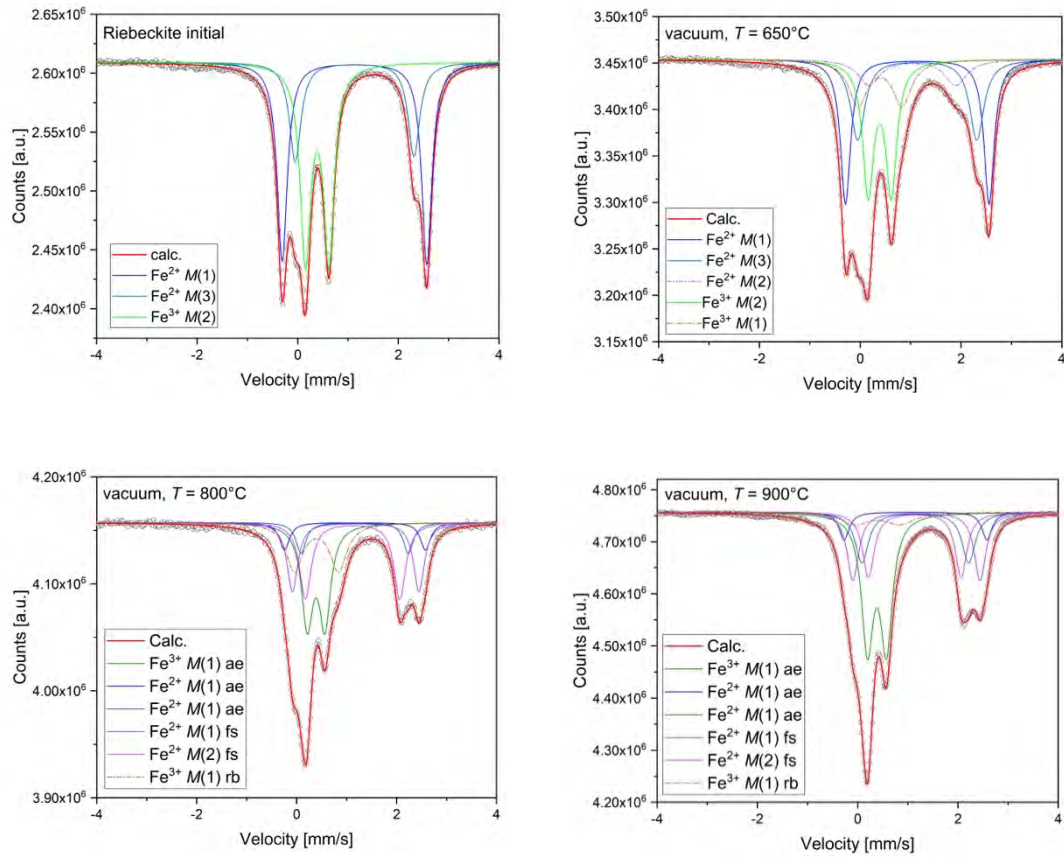


Figure 1. Selected fitted Mössbauer spectra after annealing the sample in vacuum at different temperatures; ae = aegirine, fs = ferrosilite, rb = riebeckite.

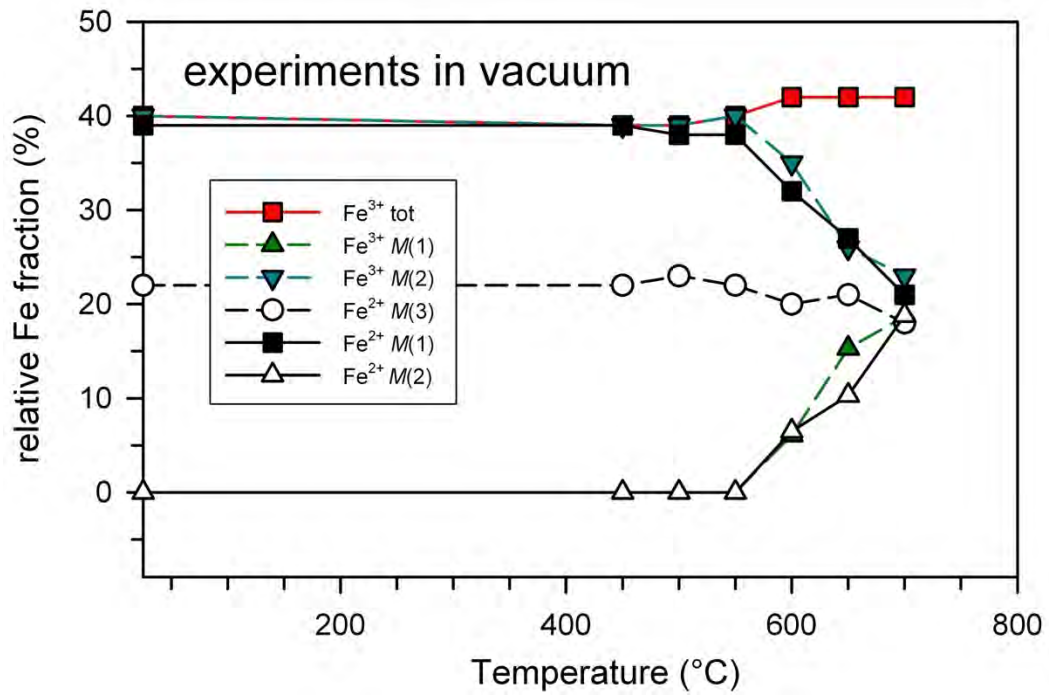


Figure 2. Evolution of the site partitioning of Fe³⁺ and Fe²⁺ in riebeckite annealed in vacuum.

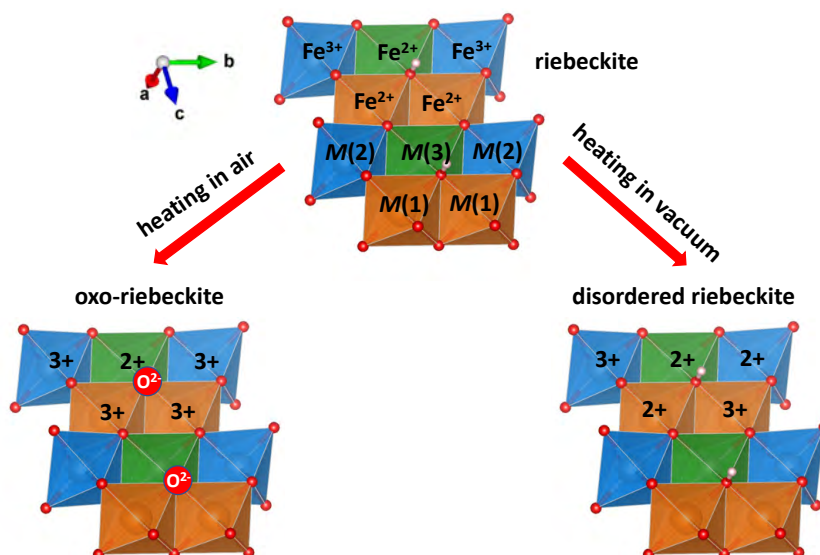


Fig. 3 Local structure within the strip of octahedra in amphiboles and schematic representation of the evolution of riebeckite at high T. In riebeckite, $M(2) = 2 \text{Fe}^{3+}$, $M(1) = 2 \text{Fe}^{2+}$ and $M(3) = \text{Fe}^{2+}$ (top); the total charge at the $M(1,3)$ sites is $6+$ and $\text{O}(3) = \text{OH}$. After heating in air, $M(2) = 2 \text{Fe}^{3+}$, $M(1) = 2 \text{Fe}^{3+}$ and $M(3) = \text{Fe}^{2+}$, hence the total charge at the $M(1,3)$ sites becomes $8+$ and $\text{O}(3) = \text{O}^{2-}$. After heating in vacuum, the site occupancies are $M(2) = (\text{Fe}^{3+}\text{Fe}^{2+})$, $M(1) = (\text{Fe}^{3+}\text{Fe}^{2+})$ and $M(3) = \text{Fe}^{2+}$; the total charge of the $M(1)M(1)M(3)$ triplet is $7+$ and local electroneutrality is achieved by changes in the individual bond distances without requiring deprotonation (see text for explanation). Drawing done using Vesta (Momma and Izumi 2008)

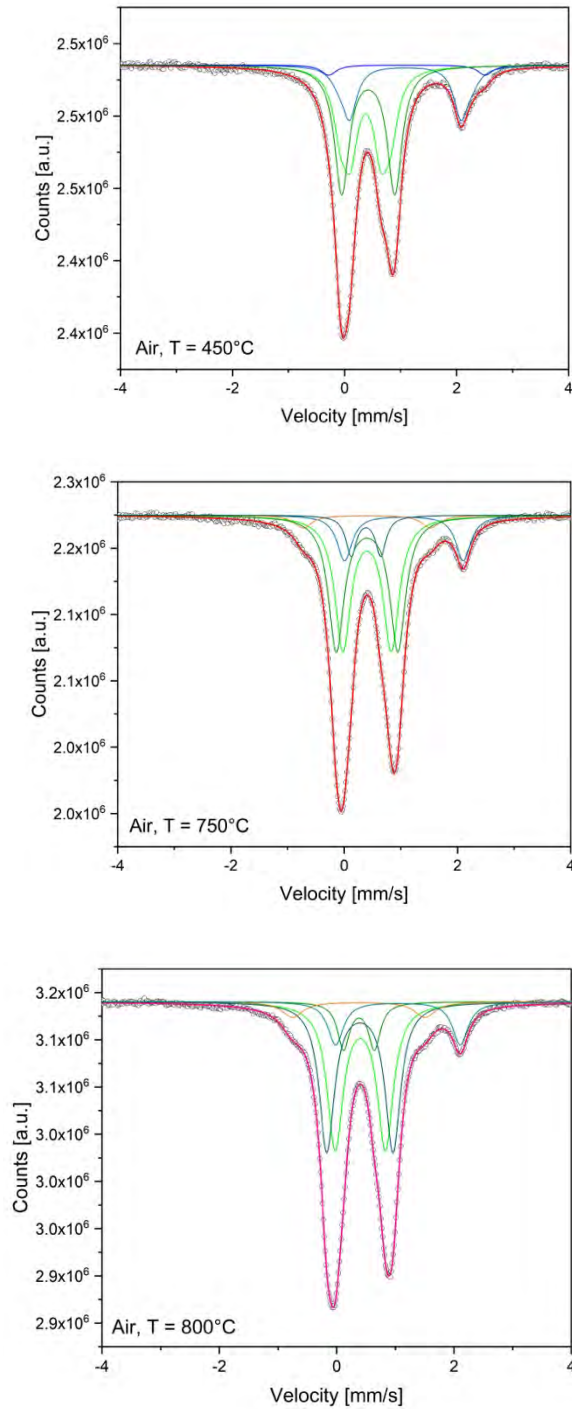


Figure 4 Fitted Mössbauer spectra after annealing the sample in air at the different temperatures.

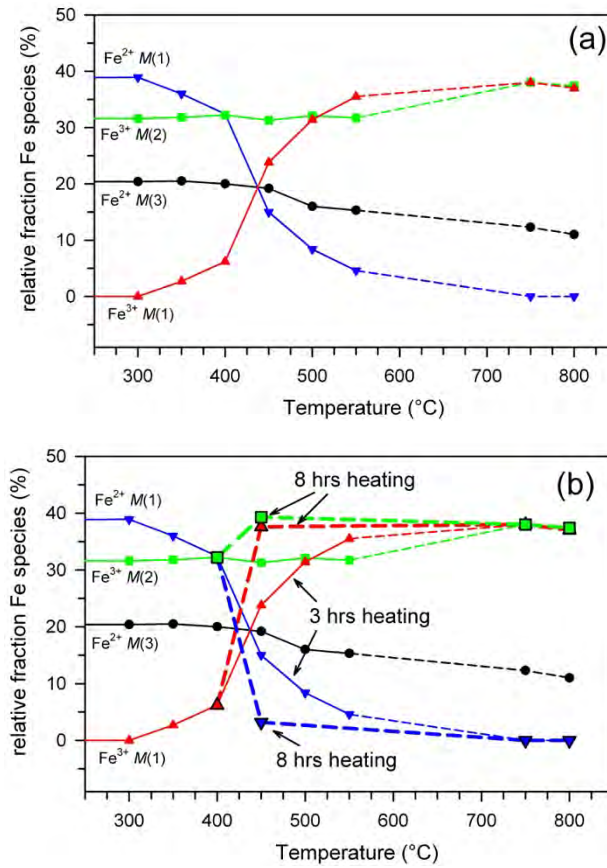


Figure 5. (a) Evolution of the Fe speciation and partitioning in riebeckite heated in air as obtained from Mössbauer analysis; data from Oberti et al. (2018) and this work (see text). (b) Same diagram as in (a) including the sample annealed at 450 °C for 8 hrs.; the strong difference in the oxidation path obtained with different annealing times is evident.

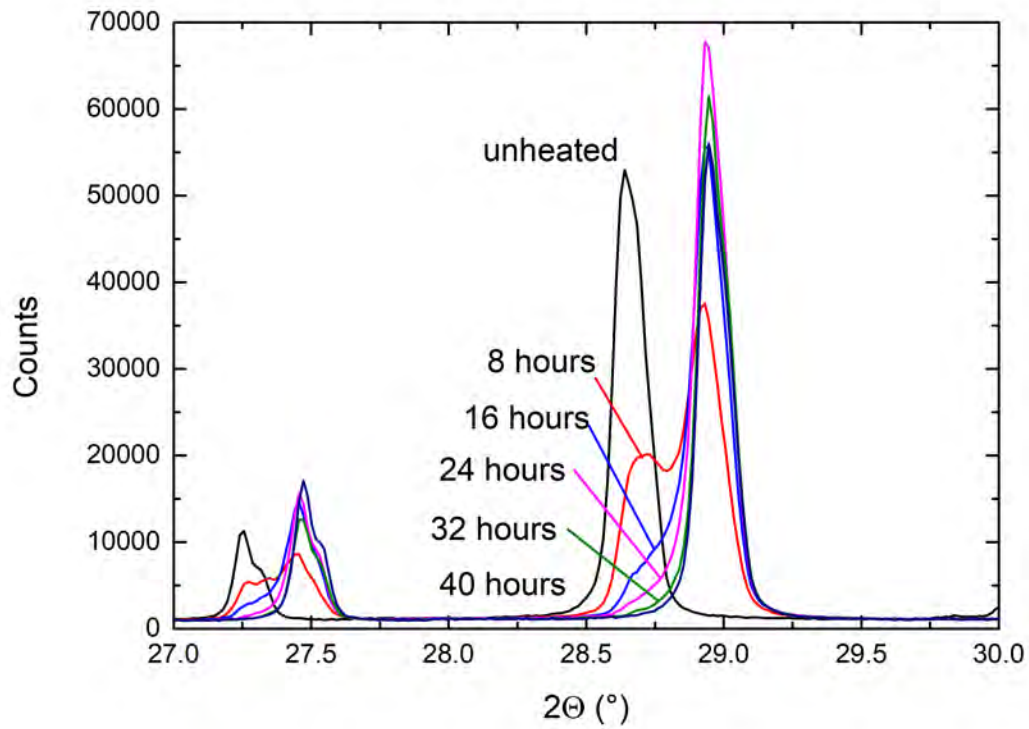


Figure 6 Evolution of the (310) peak splitting for riebeckite annealed at constant $T = 425^{\circ}\text{C}$ as a function of time. X-ray patterns collected at room-T (see text for explanation).

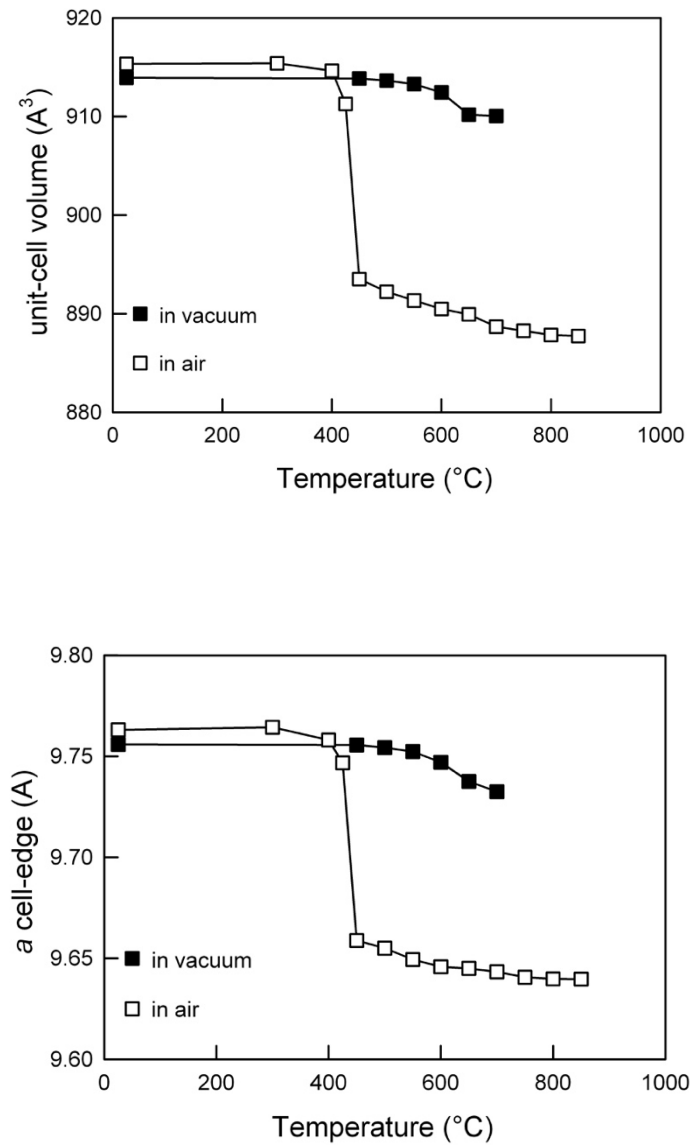


Figure 7. The distinct evolution of the unit-cell volume and the *a* cell-edge observed in riebeckite when heated in vacuum *vs.* in air.

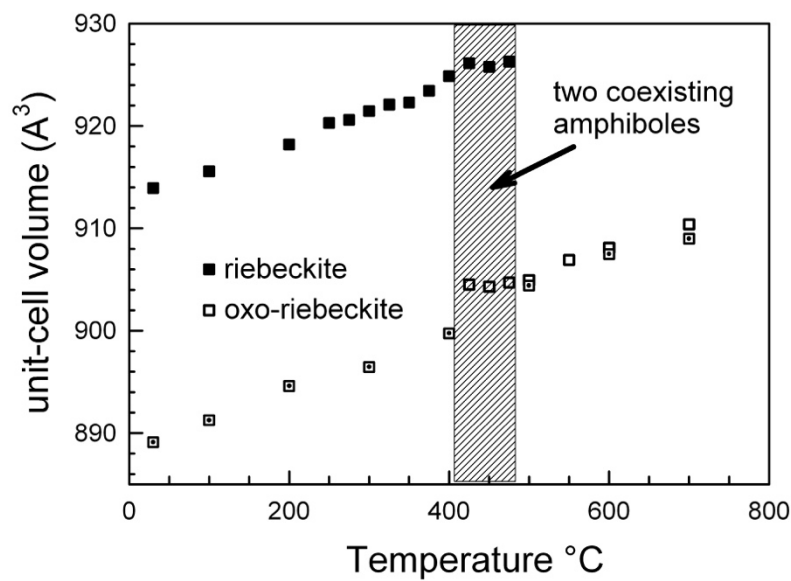
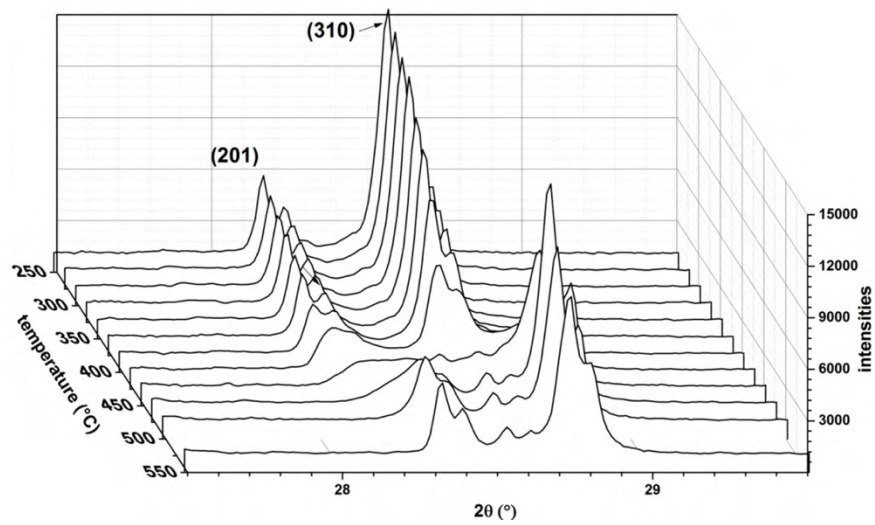


Figure 8. (a) Evolution of the XRPD pattern of riebeckite collected *in situ* in the 27-30° 2θ range as a function of temperature. (b) Evolution of the unit-cell volume measured for riebeckite powders heated in air; data collected *in situ*. The dotted empty squares were collected during cooling.

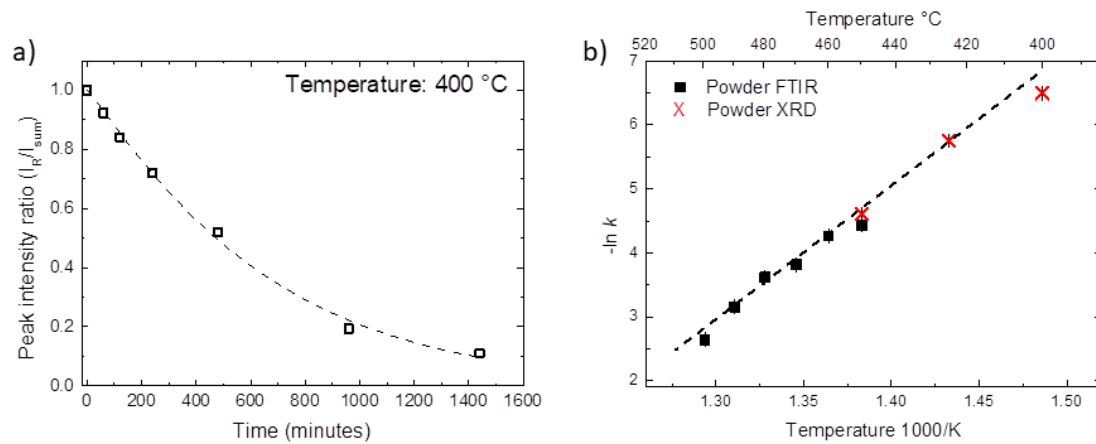


Figure 9. (a) Normalized integrated peak ratio (I_R/I_{sum}) as a function of time during the isothermal 400 °C experiments on riebeckite powder. The dashed line is the fitted the Avrami-Erofeev equation. (b) Arrhenius plot for the kinetic data measured both via FTIR (squares, from Della Ventura et al. 2021) and XRD (stars, this work). Error bars are smaller than the symbols.

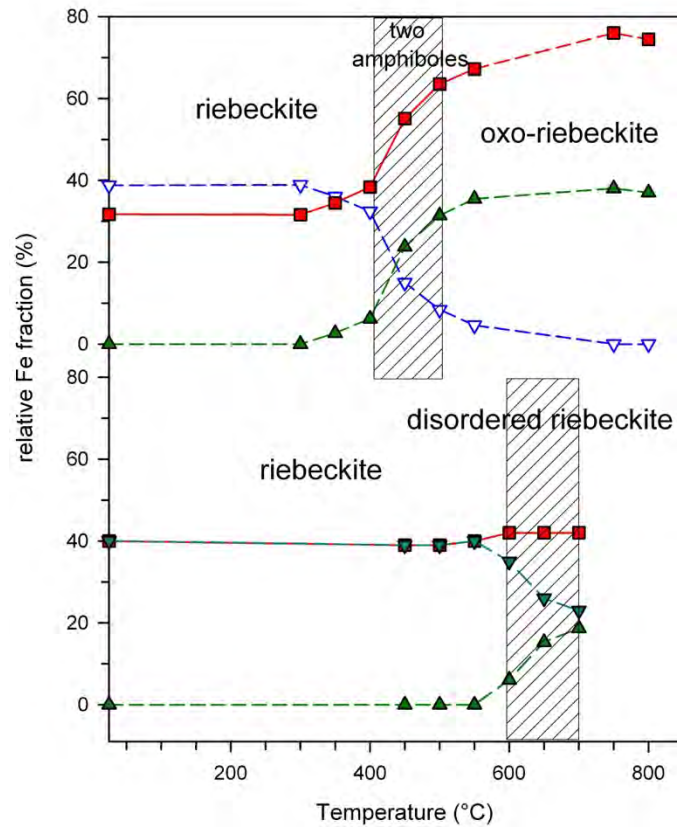


Figure 10 Evolution of the $\text{Fe}^{3+}/\text{Fe}^{2+}$ site occupancies (from Mössbauer data) in riebeckite annealed in air (data from Oberti et al. 2018, combined with those from this work) versus the $\text{Fe}^{3+}/\text{Fe}^{2+}$ site occupancies annealed in vacuum.

Supplementary material

Table S1: Refined unit-cell parameters as a function of temperature and environment.

T (°C)	<i>a</i> (Å)	<i>b</i> (Å)	<i>c</i> (Å)	β (°)	<i>Vol</i> (Å ³)	phase
Data collected after annealing in vacuum						
25	9.7559(4)	18.0582(14)	5.3368(6)	103.575(5)	913.937	rieb
450	9.7556(4)	18.0578(15)	5.3367(8)	103.577(6)	913.862	rieb
500	9.7543(4)	18.0575(16)	5.3360(9)	103.566(6)	913.650	rieb
550	9.7524(4)	18.0567(17)	5.3359(9)	103.603(7)	913.286	rieb
600	9.7471(4)	18.0558(17)	5.3343(9)	103.605(7)	912.454	rieb
650	9.7376(7)	18.0540(26)	5.3275(8)	103.636(8)	910.187	rieb
700	9.7325(8)	18.0526(33)	5.3311(17)	103.687(7)	910.060	rieb
800	9.7207(17)	18.0408(68)	5.3195(31)	104.192(29)	904.407	rieb
800	9.6698(8)	8.8137(13)	5.2815(9)	107.556(9)	429.159	ae
800	9.7248(12)	9.0342(13)	5.2428(8)	108.811(13)	436.008	fs
900	9.6780(8)	8.8248(10)	5.2876(6)	107.699(7)	430.219	ae
900	9.7282(14)	9.0319(14)	5.2442(9)	108.893(13)	435.953	fs
Data collected after annealing in air						
300	9.7644(1)	18.0697(2)	5.3365(2)	103.544(2)	915.395	rieb
400	9.7581(3)	18.0687(5)	5.3361(2)	103.552(5)	914.643	rieb
400	9.7352(4)	18.0566(12)	5.3058(4)	103.556(6)	906.693	oxo-rieb
425	9.7468(2)	18.0368(5)	5.3320(2)	103.550(3)	911.279	rieb
425	9.6748(2)	17.9868(6)	5.2985(2)	103.555(3)	896.360	oxo-rieb
450	9.6588(1)	17.9674(3)	5.2963(2)	103.564(2)	893.504	oxo-rieb
500	9.6550(2)	17.9521(3)	5.2937(2)	103.486(2)	892.235	oxo-rieb
600	9.6494(2)	17.9456(3)	5.2930(2)	103.471(2)	891.345	oxo-rieb
700	9.6458(2)	17.9402(4)	5.2915(2)	103.473(2)	890.477	oxo-rieb
800	9.6450(2)	17.9354(4)	5.2899(3)	103.466(3)	889.940	oxo-rieb
850	9.6433(1)	17.9260(4)	5.2864(2)	103.473(2)	888.690	oxo-rieb

Rieb = riebeckite, ae = aegirine, fs = ferrosilite, oxo-rieb = oxo-riebeckite